

The capabilities of the adjoint of GEOS-Chem model to support HEMCO emission inventories and MERRA-2 meteorological data

Zhaojun Tang¹, Zhe Jiang^{1*}, Jiaqi Chen¹, Panpan Yang¹, Yanan Shen¹

¹School of Earth and Space Sciences, University of Science and Technology of China, Hefei, Anhui, 230026, China.

*Correspondence to: Zhe Jiang (zhejiang@ustc.edu.cn)

Abstract

Adjoint of the GEOS-Chem model has been widely used to constrain the sources of atmospheric compositions. Here we designed a new framework to facilitate emission inventory updates in the adjoint of GEOS-Chem model. The major advantage of this new framework is good readability and extensibility, which allows us to support Harmonized Emissions Component (HEMCO) emission inventories conveniently and to easily add more emission inventories following future updates in GEOS-Chem forward simulations. Furthermore, we developed new modules to support MERRA-2 meteorological data, which allows us to perform long-term analysis with consistent meteorological data in 1979-present. The performances of the developed capabilities were evaluated with the following steps: 1) diagnostic outputs of carbon monoxide (CO) sources and sinks to ensure the correct reading and use of emission inventories; 2) forward simulations to compare the modeled surface and column CO concentrations among various model versions; 3) backward simulations to compare adjoint gradients of global CO concentrations to CO emissions with finite difference gradients; and 4) observing system simulation experiments (OSSE) to evaluate the model performance in 4D variational (4D-var) assimilations. Finally, an example application of 4D-var assimilation was presented to constrain anthropogenic CO emissions in 2015 by assimilating Measurement of Pollution in the Troposphere (MOPITT) CO observations. The capabilities developed in this work are important for better applications of the adjoint of GEOS-Chem model in the future.

31 These capabilities will be submitted to the standard GEOS-Chem adjoint code base for better
32 development of the community of the adjoint of GEOS-Chem model.

33

34 **1. Introduction**

35 GEOS-Chem is a global 3D chemical transport model (CTM) and has been widely used
36 to analyze the sources and variabilities of atmospheric compositions (Whaley et al., 2015; Li
37 et al., 2019; Hammer et al., 2020; Jiang et al., 2022). GEOS-Chem model is driven by
38 meteorological reanalysis data from the Goddard Earth Observing System (GEOS) of the
39 Global Modeling and Assimilation Office (GMAO). Emissions in GEOS-Chem model are
40 calculated with state-of-the-art inventories such as CEDS (Community Emissions Data
41 System) (Hoesly et al., 2018), MIX (Li et al., 2017) and NEI2011 (National Emissions
42 Inventory). Based on GEOS-Chem forward simulation, the adjoint of the GEOS-Chem model
43 (Henze et al., 2007) further provides the capability of backward simulation of physical and
44 chemical processes within the 4D variational (4D-var) framework. The major advantage of the
45 adjoint model is obtaining the sensitivity of atmospheric concentrations to multiple model
46 variables within a single backward simulation. The major applications of the adjoint of GEOS-
47 Chem model include inverse analyses of atmospheric composition emissions by minimizing
48 the difference between simulations and observations (Jiang et al., 2015a; Zhang et al., 2018;
49 Qu et al., 2022) as well as sensitivity analyses to analyze the sources of atmospheric
50 compositions (Jiang et al., 2015b; Zhao et al., 2019; Dedoussi et al., 2020).

51 The algorithm of the 4D-var framework requires identical model processes in the forward
52 and backward simulations. Ideally, the code for the adjoint model should be updated following
53 the GEOS-Chem forward codes to take advantage of the new features in GEOS-Chem forward
54 simulations. However, the updates in the adjoint model are difficult and usually delayed. For
55 example, the MEERA-2 meteorological reanalysis data with temporal coverage of 1979-

56 present were supported in the GEOS-Chem forward simulations in v11-01. The adjoint of
57 GEOS-Chem model does not support MERRA-2, and thus, long-term analysis must combine
58 different meteorological reanalysis data, such as GEOS-4 (1985-2007), GEOS-5 (2004-2012)
59 and GEOS-FP (2012-present). For instance, Jiang et al. (2017) constrained global carbon
60 monoxide (CO) emissions in 2001-2015, while the derived trends in CO emissions in Jiang et
61 al. (2017) could be affected by the discontinuity among various versions of the meteorological
62 data (i.e., GEOS-4 in 2001-2003, GEOS-5 in 2004-2012 and GEOS-FP in 2013-2015) and the
63 lack of consistency in the model physics of GEOS-5.

64 Emission inventories play a key role in the simulation of atmospheric compositions.
65 Harmonized Emissions Component (HEMCO) (Keller et al., 2014; Lin et al., 2021) was
66 included in the GEOS-Chem forward simulations in v10-01. HEMCO is responsible for inputs
67 of meteorological and emission data with default support for emission inventories such as
68 CEDS, MIX and NEI2011. New emission inventories can be added readily within HEMCO
69 framework. There are noticeable differences between HEMCO and the adjoint of GEOS-Chem
70 model. First, meteorological and emission data are read with individual modules in the adjoint
71 of GEOS-Chem model. Second, the inputs of emission inventories are undertaken by different
72 modules that were developed individually with significant discrepancies in the source code. In
73 addition, the file format (e.g., binary punch in the adjoint of GEOS-Chem that is the format of
74 older GEOS-Chem versions in contrast to netCDF in HEMCO), emission variables and the
75 usage methods of emission variables (e.g., emission hierarchy, scaling factors and time slice)
76 are inconsistent. These differences have posed a barrier to the application of new emission
77 inventories in the adjoint of GEOS-Chem model.

78 The lack of support to the updated emission inventories can affect the applications of the
79 adjoint of GEOS-Chem model. First, adjoint-based sensitivity analyses are obtained by the
80 backward simulations of atmospheric compositions (i.e., adjoint tracers) and the combination

81 of adjoint tracers with emissions. Out-of-date emission inventories can thus result in inaccurate
82 estimation of the adjoint sensitivities. Second, while inverse analyses are constrained by
83 atmospheric observations, the updated emission inventories are still critical because they are
84 helpful for better convergence of 4D-var assimilations by setting a more reasonable a priori
85 penalty in the cost function. For instance, the a priori biomass burning CO emissions (GFED3,
86 van der Werf et al. (2010)) in Jiang et al. (2017) lack interannual variabilities later than 2011.
87 In order to obtain reasonable convergence of biomass burning emissions, the a priori biomass
88 burning emissions in September-November 2006 were applied to September-November 2015
89 over Indonesia in Jiang et al. (2017).

90 Ideally, people should consider porting the complete HEMCO to the adjoint of GEOS-
91 Chem model to match the new features in GEOS-Chem forward simulations. However, a
92 complete port of HEMCO implies replacing the input framework of the adjoint of GEOS-Chem
93 model, as well as restructuring of HEMCO and the adjoint of GEOS-Chem model to address
94 the compatibility issues, which is very challenging and may not be necessary because the
95 meteorological modules still work well in the adjoint of GEOS-Chem model. Consequently, a
96 major objective of this work is to design a new framework to facilitate emission inventory
97 updates in the adjoint of GEOS-Chem model. For this objective, this new framework must have
98 good readability and extensibility to allow us to support HEMCO emission inventories
99 conveniently and to add more emissions inventories following future updates in GEOS-Chem
100 forward simulations easily. Furthermore, we developed new modules to support MERRA-2
101 meteorological data within the current framework of the adjoint of GEOS-Chem model, as
102 reuse of existing frameworks can save much work.

103 CO is one of the most important atmospheric pollutants and plays a key role in
104 tropospheric chemistry. Sources of atmospheric CO include fossil fuel combustion, biomass
105 burning and oxidation of hydrocarbons. The major sink of atmospheric CO is hydroxyl

106 radical (OH). The simple chemical sink of atmospheric CO allows us to simulate atmospheric
107 CO with linearized chemistry; for example, the tagged-CO mode of the GEOS-Chem model
108 can reduce the calculation cost by 98% with respect to the full chemistry mode by reading
109 archived monthly OH fields. The tagged-CO mode of the GEOS-Chem model has been widely
110 used to investigate the sources and variabilities of atmospheric CO in recent decades (Heald et
111 al., 2004; Kopacz et al., 2009; Jiang et al., 2017). The capabilities developed in this work are
112 thus based on the tagged-CO mode, as it can effectively accelerate the model development
113 process. More efforts are needed in the future to extend these capabilities to support emissions
114 inventories associated with full chemistry simulations.

115 The results presented in this paper show the development, integration, evaluation, and
116 application of these new capabilities, which is important to better applications of the adjoint of
117 GEOS-Chem model in the future. The capabilities developed in this work will be submitted to
118 the standard GEOS-Chem adjoint code base (Henze et al., 2007) for better development of the
119 community of the adjoint of GEOS-Chem model. This paper is organized as follows: in Section
120 2, we describe the adjoint of GEOS-Chem model, the development of these new capabilities,
121 and the Measurement of Pollution in the Troposphere (MOPITT) CO observations used in this
122 work. In Section 3, we evaluated the performances of the developed capabilities in forward and
123 backward simulations, together with observing system simulation experiments (OSSE) to
124 evaluate the model performance in 4D-var assimilations. An example application of 4D-var
125 assimilation to constrain anthropogenic CO emissions in 2015 by assimilating MOPITT CO
126 observations was also presented. Our conclusions follow in Section 4.

127

128 **2. Methodology and Data**

129 **2.1 Adjoint of the GEOS-Chem model**

130 We use version v35n of the adjoint of GEOS-Chem model. Our analysis is conducted at

131 a horizontal resolution of $4^\circ \times 5^\circ$ with 47 vertical levels and employs the CO-only simulation
 132 (tagged-CO mode). The global default anthropogenic emission inventory in the standard
 133 version of the adjoint of GEOS-Chem model (hereafter referred to as GC-Adjoint-STD) is
 134 Global Emissions Initiative (GEIA), but is replaced by the following regional emission
 135 inventories: NEI2008 in North America, the Criteria Air Contaminants (CAC) inventory for
 136 Canada, the Big Bend Regional Aerosol and Visibility Observational (BRAVO) Study
 137 Emissions Inventory for Mexico (Kuhns et al., 2003), the Cooperative Program for Monitoring
 138 and Evaluation of the Long-range Transmission of Air Pollutants in Europe (EMEP) inventory
 139 for Europe in 2000 (Vestreng and Klein, 2002) and the INTEX-B Asia emissions inventory for
 140 2006 (Zhang et al., 2009). Biomass burning emissions are based on the GFED3 (van der Werf
 141 et al., 2010).

142 The objective of the 4D-var approach is to minimize the difference between simulations
 143 and observations described by the cost function (Henze et al., 2007):

$$144 \quad J(\mathbf{x}) = \sum_{i=1}^N (\mathbf{F}_i(\mathbf{x}) - \mathbf{z}_i)^T \mathbf{S}_\Sigma^{-1} (\mathbf{F}_i(\mathbf{x}) - \mathbf{z}_i) + \gamma (\mathbf{x} - \mathbf{x}_a)^T \mathbf{S}_a^{-1} (\mathbf{x} - \mathbf{x}_a) \quad (1)$$

145 where \mathbf{x} is the state vector of CO emissions, N is the number of observations that are
 146 distributed in time over the assimilation period, \mathbf{z}_i is a given measurement, and $\mathbf{F}(\mathbf{x})$ is the
 147 forward model. The error estimates are assumed to be Gaussian and are given by \mathbf{S}_Σ , the
 148 observational error covariance matrix, and \mathbf{S}_a , the a priori error covariance matrix. The cost
 149 function is minimized through minimizing the adjoint gradients by adjusting the CO emissions
 150 iteratively:

$$151 \quad \nabla_{\mathbf{x}} J(\mathbf{x}) = \sum_{k=1}^N \left[2\mathbf{S}_\Sigma^{-1} (\mathbf{F}_i(\mathbf{x}) - \mathbf{z}_i) \frac{\partial \mathbf{F}_i}{\partial \mathbf{x}} \right] + 2\gamma \mathbf{S}_a^{-1} (\mathbf{x} - \mathbf{x}_a) \quad (2)$$

152 We assume a uniform observation error of 20%. The combustion CO sources (fossil fuel,
 153 biofuel and biomass burning) and the oxidation source from biogenic volatile organic
 154 compounds (VOCs) are combined, assuming a 50% uniform a priori error. We optimize the
 155 source of CO from the oxidation of methane (CH_4) separately as an aggregated global source,

156 assuming an a priori uncertainty of 25%. The CO emission estimates are optimized with
157 monthly temporal resolution. Following Jiang et al. (2017), we performed 40 iterations
158 (forward + backward simulations) for each month, which usually produced 6-8 accepted
159 iterations (i.e., successful line searches in the large-scale bound constrained optimization (L-
160 BFGS-B, Zhu et al. (1997)) to reduce the cost functions and adjoint gradients. The a posteriori
161 CO emission estimates were calculated based on the last accepted iteration, which usually
162 corresponded to the iteration with the lowest cost function.

163 **2.2 New framework to read emission inventories**

164 A major objective of this work is to design a new framework to facilitate emission
165 inventory updates in the adjoint of GEOS-Chem model. As shown in Fig. 1, we first initialize
166 the array in [INITIAL] and batch read the emission data in [READ_DATA], which were
167 interpolated offline with $1^\circ \times 1^\circ$ resolution by considering the mass conservation. Here, the data
168 include the emission inventory data listed in Table S1 (see the SI), the corresponding scaling
169 factor data and the mask map files of domain definitions. The data are scaled in
170 [SCALE_DATA] by multiplying the corresponding annual, season, month, week, and 24-hour
171 emission factors and are then online interpolated to the current resolution ($4^\circ \times 5^\circ$ in this work)
172 of the model by [RGRID_DATA], which was followed by the application of region masks in
173 [MASK].

174 The emission variable of CO obtained in this part is written to the model memory in
175 emission.f and emission_adj.f by calling DO_EMISSIONS to ensure the consistent emissions
176 in both forward and backward simulations. The GET_[TRACER] subroutines are used to
177 obtain the CO emission variable, which participates in the calculation of physicochemical
178 processes in the model, to interact with other modules. Finally, the variable is cleaned from the
179 memory by the [CLEANUP] module. It should be noted that a two-step interpolation is
180 employed in this work (hereafter referred to as GC-Adjoint-HEMCO) following GC-Adjoint-

181 STD, for example, $0.1^{\circ} \times 0.1^{\circ}$ to $1^{\circ} \times 1^{\circ}$ and then to $4^{\circ} \times 5^{\circ}$ for the NEI2011 inventory, which is
182 different from the one-step interpolation in GEOS-Chem forward model (v12-08-01, hereafter
183 referred to as GC-v12), for example, $0.1^{\circ} \times 0.1^{\circ}$ to $4^{\circ} \times 5^{\circ}$ directly for the NEI2011 inventory.
184 The different interpolation methods can lead to differences in the interpolated emission data.

185 **2.3 Updates in emission inventories**

186 In addition to baseline emission data, there are critical factors that affect the usage of
187 emission data in the models. Reading the emission data correctly thus does not necessarily
188 mean using emission data correctly. For example, emission hierarchy is used to prioritize
189 emission fields within the same emission category. Emissions of higher hierarchy overwrite
190 lower hierarchy data. Regional emission inventories usually have a higher hierarchy within
191 their mask boundaries. Scaling factors are used to adjust the baseline emissions with annual,
192 season, month, week, and 24-hour temporal scales. Time slice selection is used to define the
193 usage methods of the emission data outside the original temporal range; for instance, data can
194 be interpreted as climatology and recycled once the end of the last time slice is reached or be
195 only considered as long as the simulation time is within the time range. Furthermore, there are
196 experience parameters applied in files such as `emfossil.f` and `tagged_co.f`, which may not be
197 compatible with HEMCO emission inventories. Consequently, we must validate the integrated
198 emissions carefully to ensure that the abovementioned factors have been correctly applied and
199 to ensure that the calculated emissions are reasonable for individual inventories and the
200 combination of all inventories.

201 To take advantage of this new framework, six HEMCO emission inventories have been
202 added to this work. To validate the emissions, we performed actual simulations with GC-v12,
203 GC-Adjoint-HEMCO and GC-Adjoint-STD, and the emissions were calculated in the model
204 simulations and then output to the Log file. As shown in Table S1, the CEDS emission
205 inventory ($0.5^{\circ} \times 0.5^{\circ}$) is adopted in GC-Adjoint-HEMCO to provide global default emissions

206 for 1750-2019. The diurnal scale factors are applied to obtain CO emissions at different
207 moments of the day. Fig. S1 (see the SI) shows CEDS CO emissions in 2015 in GC-v12 and
208 GC-Adjoint-HEMCO and GEIA CO emissions in GC-Adjoint-STD, and we find noticeable
209 differences in CO emissions between CEDS and GEIA. As shown in Table 1, the CEDS CO
210 emissions in 2015 were 613.57 and 613.85 Tg/y in GC-v12 and GC-Adjoint-HEMCO,
211 respectively, with a relative difference of 0.05% between GC-v12 and GC-Adjoint-HEMCO.
212 The GEIA CO emissions in 2015 were 445.88 Tg/year in GC-Adjoint-STD.

213 The default CEDS inventory is replaced by the following regional emission inventories
214 in GC-Adjoint-HEMCO: MIX in Asia ($0.25^{\circ} \times 0.25^{\circ}$), NEI2011 in the United States
215 ($0.1^{\circ} \times 0.1^{\circ}$), DICE_AFRICA and EDGARV43 in Africa ($0.1^{\circ} \times 0.1^{\circ}$) and APEI in Canada
216 ($0.1^{\circ} \times 0.1^{\circ}$). As shown in Fig. S2 (see the SI), the MIX inventory provides Asian emissions in
217 2008-2010, accompanied by diurnal scale factors to describe daily emission variation. The
218 $1^{\circ} \times 1^{\circ}$ scale factors in the AnnualScalar.geos.1x1.nc file further provide the annual variation in
219 1985-2010. As shown in Table 1, the MIX CO emissions in 2015 were 321.18 and 321.71 Tg/y
220 in GC-v12 and GC-Adjoint-HEMCO, respectively, with a relative difference of 0.17% between
221 GC-v12 and GC-Adjoint-HEMCO. The INTEX-B CO emissions in 2015 were 353.03 Tg/y in
222 GC-Adjoint-STD.

223 The NEI2011 inventory (Fig. S3, see the SI) provides anthropogenic emissions for the
224 United States in 2011 with annual scalar factors from 2006-2013. The weekday and weekend
225 factors are read from NEI99.dow.geos.1x1.nc file since 1999 with all CO factors of 1.0 on
226 weekdays and between 0.990 and 0.997 on Saturdays and Sundays. The NEI2011 CO
227 emissions in 2015 were 35.83 and 37.70 Tg/y in GC-v12 and GC-Adjoint-HEMCO,
228 respectively, with a relative difference of 5.22% between GC-v12 and GC-Adjoint-HEMCO.
229 The NEI2008 CO emissions in 2015 were 52.87 Tg/y in GC-Adjoint-STD. APEI (Fig. S4, see
230 the SI) is the primary source of anthropogenic emissions in the Canadian domain. The APEI

231 CO emissions in 2015 were 6.10 and 6.17 Tg/y in GC-v12 and GC-Adjoint-HEMCO,
232 respectively, with a relative difference of 1.14% between GC-v12 and GC-Adjoint-HEMCO.
233 The CAC CO emissions in 2015 were 10.20 Tg/y in GC-Adjoint-STD. Following GC-v12, the
234 CO emissions in APEI are enhanced by 19% to account for coemitted VOC in the tagged-CO
235 simulation.

236 Emissions for the African domain are provided by the combination of DICE_AFRICA
237 and EDGARV43 (Fig. S5, see the SI). Here DICE_AFRICA includes anthropogenic and
238 biofuel emissions in 2013. We read the DICE_AFRICA emissions data into the model in two
239 types according to the guidelines of the inventory. Emissions from sectors such as automobiles
240 and motorcycles are aggregated into anthropogenic sources, and household-generated
241 emissions such as charcoal and agricultural waste are aggregated into biofuel sources. Efficient
242 combustion emissions from EDGAR v4.3 in 1970-2010 then compensate for the lacking
243 sources in DICE_AFRICA. Daily variation factors for CO are also used here for emissions
244 across the African region. The 2010 CO seasonal scale factors are used in EDGAR v4.3 for
245 sectoral emission sources. The DICE_AFRICA and EDGARV43 CO emissions in 2015 were
246 83.42 and 83.02 Tg/y in GC-v12 and GC-Adjoint-HEMCO, respectively, with a relative
247 difference of -0.48% between GC-v12 and GC-Adjoint-HEMCO. Following GC-v12, the CO
248 emissions in DICE_AFRICA and EDGARV43 are enhanced by 19% to account for coemitted
249 VOC in the tagged-CO simulation.

250 The biomass burning emission inventory in GC-Adjoint-HEMCO is GFED4 (Fig. S6,
251 see the SI), which includes dry matter emissions from a total of seven sectors in 1997-2019.
252 The same GFED_emission_factors.H header file as in the GC-v12 version is read in the GC-
253 Adjoint-HEMCO. This file contains the ratio factors of atmospheric pollutants, and we
254 multiply the ratio factors one by one according to the ID of each species to ensure that the
255 species in the model have biomass burning sources. The GFED4 CO emissions in 2015 were

256 437.13 and 435.89 Tg/y in GC-v12 and GC-Adjoint-HEMCO, respectively, with a relative
257 difference of -0.28% between GC-v12 and GC-Adjoint-HEMCO. The GFED3 CO emissions
258 in 2015 were 382.04 Tg/year in GC-Adjoint-STD. Following GC-v12, the combustion CO
259 sources in biomass burning are enhanced by 5% to consider the CO generated by VOC in the
260 tagged-CO simulation.

261 Fig. 2 shows the total combustion CO emissions in 2015 from GC-v12, GC-Adjoint-
262 HEMCO and GC-Adjoint-STD. As shown in Table 2, the regional combustion CO emissions
263 are 320.66 and 320.38 Tg/y (Asia), 73.96 and 66.93 Tg/y (North America), 199.51 and
264 193.29/y Tg (Africa), 79.04 and 78.91 Tg/y (South America), 31.58 and 30.96 Tg/y (Europe)
265 and 12.24 and 11.99 Tg/y (Australia) in GC-v12 and GC-Adjoint-HEMCO, respectively. Fig.
266 3 further shows the monthly combustion CO emissions in 2015 from GC-v12, GC-Adjoint-
267 HEMCO and GC-Adjoint-STD, and there are good agreements in the monthly variation of CO
268 emissions between GC-v12 and GC-Adjoint-HEMCO. The CO emissions in GC-Adjoint-STD
269 are similar to those in GC-v12 and GC-Adjoint-HEMCO in winter and spring but with large
270 differences in summer and autumn. This seasonal difference may reflect the influence of
271 different emission inventories on biomass burning.

272 **2.4 Updates in CO chemical sources and sinks**

273 The biogenic emissions in GC-Adjoint-STD are Model of Emissions of Gases and
274 Aerosols from Nature, version 2.0 (MEGANv2.0, Guenther et al. (2006)) in the full chemistry
275 simulation but are GEIA in the tagged-CO simulation (Fig. S7, see the SI). Fisher et al. (2017)
276 demonstrated improvement in modeled CO concentrations in tagged-CO simulation by reading
277 archived VOC- and CH₄-generated CO fields provided by full chemistry simulation. The
278 archived VOC- and CH₄-generated CO fields in 2013 (PCO_3Dglobal.geosfp.4x5.nc) were set
279 as the default CO chemical sources in the tagged-CO simulation in GC-v12 and supported in
280 GC-Adjoint-HEMCO. As shown in Table 2, the CO chemical sources (columns) obtained by

281 reading the archived VOC- and CH₄-generated CO fields demonstrate good agreement between
282 GC-v12 and GC-Adjoint-HEMCO. However, they are 30-60% lower than those in GEIA in
283 GC-Adjoint-STD, and this difference could be partially associated with the inconsistency
284 between the archived VOC-generated CO fields in 2013 and the actual meteorological data in
285 2015 in the simulation.

286 The default CH₄-generated CO emissions in GC-Adjoint-STD (Fig. S8, see the SI) are
287 calculated based on averaged CH₄ concentrations in four latitude bands (90°S - 30°S, 30°S -
288 00°S, 00°N - 30°N, 30°N - 90°N), which are based on Climate Monitoring and Diagnostics
289 Laboratory (CMDL) surface observations and Intergovernmental Panel on Climate Change
290 (IPCC) future scenarios. As shown in Table 2, there are good agreements in the CH₄-generated
291 CO emissions between GC-v12 and GC-Adjoint-HEMCO by reading
292 PCO_3Dglobal.geosfp.4x5.nc, and they are 20-60% lower than those in CMDL/IPCC in GC-
293 Adjoint-STD. Furthermore, the default archived monthly OH fields were updated following
294 GC-v12 with updated calculations for the decay rate (KRATE, from JPL 03 to JPL 2006) in
295 GC-Adjoint-HEMCO. The subsequent CO sinks (Fig. S9, see the SI) in GC-v12 and GC-
296 Adjoint-HEMCO are 20-40% higher than those in GC-Adjoint-STD.

297 **2.5 Updates in meteorological data**

298 The MERRA-2 meteorological data (1979-present) are supported in GC-Adjoint-
299 HEMCO to ensure long-term consistency in the meteorological data in the analyses. The code
300 porting to support MERRA-2 follows the current framework of the adjoint of GEOS-Chem
301 model, particularly because the meteorological variables and vertical resolutions of MERRA-
302 2 are the same as those of GEOS-FP (2012-present), while GEOS-FP is already supported by
303 GC-Adjoint-STD. Fig. 4A-B show the averages of surface CO concentrations in 2015 from
304 GC-Adjoint-HEMCO driven by MERRA-2 and GEOS-FP, respectively. Our results
305 demonstrate lower surface CO concentrations driven by MERRA-2 (Fig. 4C), although there

306 is good agreement in the spatial distributions of CO concentrations. Similarly, Fig. 4D-F show
307 the averages of CO columns in 2015 from GC-Adjoint-HEMCO driven by MERRA-2 and
308 GEOS-FP and their differences. Despite the noticeable differences in surface CO
309 concentrations (Fig. 4C), the differences in CO columns (Fig. 4F) are much smaller, and the
310 modeled CO columns driven by MERRA-2 are higher than those driven by GEOS-FP over the
311 Indian Ocean. The discrepancy between surface and column CO in Fig. 4 may reflect the
312 impacts of different convective transports on the modeled CO concentrations.

313 **2.6 MOPITT CO measurements**

314 The MOPITT data used here were obtained from the joint retrieval (V7J) of CO from
315 thermal infrared (TIR, 4.7 μ m) and near-infrared (NIR, 2.3 μ m) radiances using an optimal
316 estimation approach (Worden et al., 2010; Deeter et al., 2017). The retrieved volume mixing
317 ratios (VMR) are reported as layer averages of 10 pressure levels with a footprint of 22 km \times
318 22 km. Following Jiang et al. (2017), we reject MOPITT data with CO column amounts less
319 than 5×10^{17} molec/cm² and with low cloud observations. Since the NIR channel measures
320 reflected solar radiation, only daytime data are considered.

321

322 **3. Model evaluation and application**

323 **3.1 Model performances in forward and backward simulations**

324 The reasonable emissions in the diagnostic outputs in Section 2 do not necessarily mean
325 the correct integration of emissions in the assimilations. Consequently, here we evaluate the
326 performance of GC-Adjoint-HEMCO in forward simulations. Fig. 5 shows the averages of
327 surface and column CO concentrations in 2015 from GC-v12, GC-Adjoint-HEMCO and GC-
328 Adjoint-STD. As shown in Table 2, the regional differences between GC-v12 and GC-Adjoint-
329 HEMCO are 2.6%, -5.7%, -4.6%, -1.7%, -1.4% and -3.6% in surface CO concentrations, and
330 -2.3%, -3.6%, -3.3%, -3.1%, -3.3% and -4.1% in CO columns over Asia, North America,

331 Africa, South America, Europe, and Australia, respectively. There are larger regional
 332 differences in CO concentrations between GC-v12 and GC-Adjoint-STD: 4.6%, -10.1%, 6.3%,
 333 22.5%, 6.4% and 25.7% in surface CO concentrations, and -0.7%, -9.9%, 2.5%, 8.0%, -5.8%
 334 and 8.5% in CO columns over Asia, North America, Africa, South America, Europe, and
 335 Australia, respectively. The agreement between GC-v12 and GC-Adjoint-HEMCO confirms
 336 the reliability of GC-Adjoint-HEMCO in forward simulations, while the small differences in
 337 CO concentrations between GC-v12 and GC-Adjoint-HEMCO are expected in view of the
 338 comparable differences in regional emissions, chemical sources and sinks, as shown in Table
 339 2.

340 In addition to forward simulations, the reliability of 4D-var assimilation also relies on
 341 the accuracy of the adjoint-based sensitivities, which are obtained by the backward simulations
 342 of adjoint tracers and the combination of adjoint tracers with emissions. As mentioned in
 343 Section 2.2, we have made corresponding modifications to both forward and backward
 344 modules. Consequently, here we further evaluate the performance of GC-Adjoint-HEMCO in
 345 backward simulations. Here the adjoint gradients are simplified as:

$$346 \quad \nabla_x J(\mathbf{x}) = \frac{\partial F_N}{\partial \mathbf{x}} \quad (3)$$

347 The adjoint gradients (Eq. 3) represent the sensitivities of modeled atmospheric compositions
 348 at the final time step (i.e., $i = N$) to emissions, which were then compared with the finite
 349 difference gradients calculated with:

$$350 \quad \Lambda = \frac{J(\sigma + \delta\sigma) - J(\sigma - \delta\sigma)}{2\delta\sigma} \quad (4)$$

351 Here the finite difference gradients represent the response of modeled atmospheric
 352 compositions at the final time step to finite perturbations in emissions provided by the forward
 353 simulations ($\delta\sigma = 10\%$ in this work).

354 Fig. 6A-C show the comparison of adjoint and finite difference gradients of global CO
 355 concentrations to CO emissions with a 24-hour assimilation window by turning on the

356 convection, planetary boundary layer mixing and advection processes individually. We find
357 good consistency in the gradients with respect to convection and planetary boundary layer
358 mixing. The larger deviation with respect to advection is caused by the discrete advection
359 algorithm in forward simulations and continuous advection algorithm in backward simulations
360 (Henze et al., 2007). Fig. 6D-F further exhibit the effects of combined model processes (turning
361 off advection as suggested by Henze et al. (2007)). We find good agreement between the
362 adjoint and finite difference gradients with different assimilation windows (24 hours, 7 days
363 and one month). This confirms the consistency in the impacts of emissions to modeled
364 atmospheric compositions between the forward and backward simulations, which is the
365 prerequisite for more detailed evaluations in the following Sections.

366 **3.2 Observing system simulation experiments with pseudo-CO observations**

367 Here we further evaluate the performance of GC-Adjoint-HEMCO in 4D-var
368 assimilations. OSSE is a useful method and has been widely used to evaluate the performance
369 of various data assimilation systems (Jones et al., 2003; Barré et al., 2015; Shu et al., 2022). In
370 contrast to assimilations by assimilating actual atmospheric observations, pseudo-observations
371 are usually generated by model simulations and then assimilated in OSSE. The true
372 atmospheric states are known in OSSEs as they are used to produce the pseudo-observations,
373 and consequently, the difference between assimilated and true atmospheric states describes the
374 capability of the assimilation systems to converge to the true atmospheric states in assimilations
375 when assimilating actual observations.

376 The pseudo-observations in this work are produced by archiving CO concentrations from
377 GC-Adjoint-HEMCO forward simulations with the CO emissions unchanged (i.e., the default
378 CO emission inventory such as CEDS, MIX and NEI2011). According to the usage of pseudo-
379 observations, two types of OSSE are performed in this work: 1) full modeled CO fields are
380 assimilated as pseudo-observations so that we have pseudo-CO observations at every grid/level

381 and time step (hereafter referred to as OSSE-FullOBS). This experiment is designed to evaluate
382 the performance of the assimilation system under ideal conditions with full coverage of
383 observations. 2) The modeled CO fields are sampled at the locations/times of MOPITT CO
384 observations and smoothed with MOPITT a priori concentrations and averaging kernels to
385 produce MOPITT-like pseudo-CO observations (hereafter referred to as OSSE-MOPITT). This
386 experiment is designed to evaluate the performance of the assimilation system under actual
387 conditions with limited coverage of observations.

388 In the inverse analysis with the pseudo-CO observations, we reduce the anthropogenic
389 CO emissions by 50% so that the objective of the OSSE is to produce scaling factors that can
390 return the source estimate to the default emissions (i.e., scaling factors of 1.0). Fig. 7A shows
391 the annual scaling factors in 2015 in OSSE-FullOBS. After 40 iterations, the a posteriori
392 anthropogenic CO emission estimates converge to the true states in all major emission regions.
393 As shown in Table 3, the regional scaling factors of OSSE-FullOBS are 1.00, 0.97, 0.97, 1.00,
394 0.98 and 0.94 for anthropogenic CO emissions over Asia, North America, Africa, South
395 America, Europe, and Australia, respectively.

396 Furthermore, Fig. 7D shows the annual scaling factors in OSSE-MOPITT, which are
397 noticeably worse than those in Fig. 7A. The regional scaling factors of OSSE-MOPITT are
398 1.04, 0.88, 1.01, 1.02, 0.84 and 0.81 for anthropogenic CO emissions over Asia, North
399 America, Africa, South America, Europe, and Australia, respectively. With respect to OSSE-
400 FullOBS, the limited coverage of observations in OSSE-MOPITT has resulted in
401 approximately 15% underestimations in the a posteriori CO emission estimates over North
402 America and Europe. In addition, Fig. 7B-C and Fig. 7E-F show the a priori and a posteriori
403 biases in the modeled CO columns. We find dramatic improvements in the modeled CO
404 columns, which confirms the reliability of the 4D-var assimilation system. The difference
405 between Fig. 7B and 6E reflects the influence of the application of MOPITT averaging kernels,

406 which lead to larger negative biases in the a priori simulation. It should be noted that we cannot
407 expect comparable improvement in the actual assimilations because of the potential effects of
408 model and observation errors.

409 **3.3 Anthropogenic CO emissions constrained with MOPITT CO observations**

410 As an example of the application of GC-Adjoint-HEMCO, here we constrain
411 anthropogenic CO emissions in 2015 by assimilating MOPITT CO observations. Fig.8A shows
412 the relative differences between modeled and MOPITT CO columns at the beginning of each
413 month in 2015 (i.e., biases in monthly initial CO conditions) in the original GEOS-Chem
414 simulations. We find dramatic underestimations in the modeled CO columns by approximately
415 30-40%. As indicated by previous studies (Jiang et al., 2013; Jiang et al., 2017), the biases in
416 monthly initial CO conditions are caused by model biases in CO concentrations accumulated
417 in previous months. Considering that the lifetime of CO is approximately 2-3 months, the
418 negative biases in the initial conditions can result in negative biases in the modeled CO
419 concentration in the following month. A lack of consideration of these biases, as shown in Fig.
420 8A, can thus result in overestimations in the derived monthly CO emission estimates because
421 the assimilation system will tend to adjust emissions to reduce the initial condition-induced
422 biases.

423 Following Jiang et al. (2017), a suboptimal sequential Kalman filter (Todling and Cohn,
424 1994; Tang et al., 2022) was employed in this work to optimize the modeled CO concentrations
425 with an hourly resolution by combining GC-Adjoint-HEMCO forward simulation and
426 MOPITT CO observations. The CO concentrations provided by the Kalman filter assimilations
427 were archived at the beginning of each month, which were used as the optimized monthly initial
428 CO conditions in the inverse analysis. As shown in Fig. 8B, the biases in the modeled CO
429 columns in the optimized initial CO conditions are pronounced lower than those in the original
430 simulation (Fig. 8A). The optimization of the initial CO conditions is essential for our inverse

431 analysis, as it can ensure that the adjustments in CO emissions are dominated by the differences
432 between simulations and observations in the current month instead of the 30-40%
433 underestimations in CO columns accumulated in previous months.

434 Fig. 9A shows the distribution of a priori anthropogenic CO emissions in 2015. The
435 regional a priori anthropogenic CO emissions (as shown in Table 4) are 243.53, 34.42, 23.24,
436 30.39, 25.94 and 2.02 Tg/y over Asia, North America, Africa, South America, Europe, and
437 Australia, respectively. As shown in Fig. 9B, our inverse analysis suggests a wide distribution
438 of underestimations in the a priori anthropogenic CO emissions in 2015 except in E. China.
439 The regional scaling factors (Table 4) are 1.16, 1.47, 1.52, 1.41, 1.60 and 1.38, and the a
440 posteriori anthropogenic CO emissions are 283.20, 50.47, 35.34, 42.92, 41.62 and 2.79 Tg/y
441 over Asia, North America, Africa, South America, Europe, and Australia, respectively. As
442 shown in Fig. 9C, we find noticeable underestimations in the modeled CO columns in the a
443 priori simulations, despite the negative biases being much weaker than those in Fig. 8A due to
444 the optimization of the initial CO conditions. The negative biases are effectively reduced in the
445 a posteriori simulation driven by the a posteriori CO emission estimates (Fig. 9D).

446 Finally, we compare the a posteriori CO emission estimates in this work with Jiang et al.
447 (2017), who constrained CO emissions in 2001-2015 with GC-Adjoint-STD by assimilating
448 the same MOPITT CO observations. As shown in Table 4, the a posteriori anthropogenic CO
449 emission estimates in this work match well with Jiang et al. (2017) in North America and Africa
450 but are 38%, 157% and 228% higher than those in Jiang et al. (2017) in Asia, South America
451 and Australia, respectively. A major discrepancy between this work and Jiang et al. (2017) is
452 the treatment of ocean grids. Jiang et al. (2017) defined ocean grids as continental boundary
453 conditions, which were rewritten hourly using the optimized CO concentrations archived from
454 the suboptimal sequential Kalman filter by assimilating MOPITT CO observations. Only
455 MOPITT data over land were assimilated in the 4D-var assimilations in Jiang et al. (2017)

456 without any change in CO distribution over the ocean. In addition, the large differences in
457 chemical sources and sinks between GC-Adjoint-HEMCO and GC-Adjoint-STD, for example,
458 lower VOC-generated CO emissions by 40-60% and higher CO sinks by 20-40% in GC-
459 Adjoint-HEMCO, as shown in Table 2, may also contribute to the discrepancy in the derived
460 a posteriori CO emission estimates.

461 As shown in Fig. 9D, the a posteriori simulation demonstrates positive biases in CO
462 columns over China and Southeast Asia, which is a signal of overestimated local CO emissions;
463 meanwhile, the negative biases over the northern Pacific Ocean are reduced in the a posteriori
464 simulation. The negative biases over the remote ocean are more affected by CO chemical
465 sources and sinks; however, biases in chemical sources cannot be effectively adjusted because
466 of the global uniform scaling factor for CH₄-generated CO emissions; biases in chemical sinks
467 cannot be adjusted because of the fixed OH fields in the tagged-CO simulation. Jiang et al.
468 (2017) tried to address this problem by defining continental boundary conditions so that the
469 inverse analysis is dominated by local MOPITT observations to avoid the influence of model
470 biases accumulated within the long-range transport. Conversely, CO emissions over China and
471 Southeast Asia are overestimated in this work to offset the negative biases over the northern
472 Pacific Ocean. We expect similar overestimations in the a posteriori CO emission estimates
473 over South America, southern Africa, and Australia in this work because it is the effective
474 pathway to reduce the negative bias over the ocean in the Southern Hemisphere.

475 **4. Conclusion**

476 This work demonstrates our efforts on the development of a new framework to facilitate
477 emission inventory updates in the adjoint of GEOS-Chem model. The major advantage of this
478 new framework is good readability and extensibility, which allows us to conveniently support
479 HEMCO emission inventories, including CEDS, MIX, NEI2011, DICE_AF, AF_EDGAR43,
480 APEI and GFED4. The updated emission inventories are critical for reliable sensitivity

481 analyses, as well as better convergence of assimilations by setting a more reasonable a priori
482 penalty in the cost function. Second, we developed new modules to support MERRA-2
483 meteorological data, which allows us to perform long-term inverse analysis with consistent
484 meteorological data in 1979-present. We evaluated the performances of the developed
485 capabilities by validating the diagnostic outputs of CO emissions, modeled surface and column
486 CO concentrations in forward simulations, and adjoint gradients of global CO concentrations
487 to CO emissions with respect to the finite difference gradients.

488 Two types of OSSE were conducted to evaluate the model performance in 4D-var
489 assimilations. The a posteriori CO emissions converged to the true states in all major emission
490 regions with fully covered pseudo-CO observations; the limited coverage of observations by
491 sampling the pseudo-CO observations at the locations/times of MOPITT CO observations and
492 smoothing with MOPITT averaging kernels resulted in approximately 15% underestimations
493 in the a posteriori CO emissions over North America and Europe. Furthermore, as an example
494 application of the developed capabilities, we constrain anthropogenic CO emissions in 2015
495 by assimilating MOPITT CO observations. The a posteriori anthropogenic CO emission
496 estimates derived in this work match well with Jiang et al. (2017) in North America and Africa
497 but are overestimated in Asia, South America and Australia, which could be associated with
498 the different treatment of MOPITT CO observations over ocean grids and the large differences
499 in CO chemical sources and sinks. The capabilities developed in this work are a useful
500 extension for the adjoint of GEOS-Chem model. More efforts are needed to support emissions
501 inventories associated with full chemistry simulations, as well as integration of these
502 capabilities with the standard GEOS-Chem adjoint code base for better development of the
503 community of the adjoint of GEOS-Chem model.

504

505 **Code and data availability:** The MOPITT CO data can be downloaded from
506 <https://asdc.larc.nasa.gov/data/MOPITT/>. The GEOS-Chem model (version 12.8.1) can be
507 downloaded from http://wiki.seas.harvard.edu/geos-chem/index.php/GEOS-Chem_12#12.8.1.
508 The adjoint of GEOS-Chem model (GC-Adjoint-STD) can be downloaded from
509 http://wiki.seas.harvard.edu/geos-chem/index.php/GEOS-Chem_Adjoint. The adjoint of
510 GEOS-Chem model (GC-Adjoint-HEMCO) can be downloaded from
511 <https://doi.org/10.5281/zenodo.7512111>.

512

513 **Author Contributions:** Z.J. designed the research. Z.T. developed the model code and
514 performed the research. Z.J. and Z.T. wrote the manuscript. All authors contributed to
515 discussions and editing the manuscript.

516

517 **Competing interests:** The authors declare that they have no conflicts of interest.

518

519 **Acknowledgments:** We thank the providers of the MOPITT CO data. The numerical
520 calculations in this paper have been done on the supercomputing system in the Supercomputing
521 Center of University of Science and Technology of China. This work was supported by the
522 Hundred Talents Program of Chinese Academy of Science and National Natural Science
523 Foundation of China (42277082, 41721002).

524

525 **Tables and Figures**

526 **Table 1.** CO emissions for each inventory in 2015 with unit Tg/y.

527

528 **Table 2.** Regional combustion CO emissions, VOC-generated CO (PCO_NMVOC), CH₄-
529 generated CO (PCO_CH₄), CO sinks (CO_OH, calculated as CO_OH = KRATE×CO×OH),
530 and simulated surface and column CO concentrations in 2015. The region definitions are shown
531 in Fig. 2A.

532

533 **Table 3.** Annual scaling factors of anthropogenic CO emissions in OSSEs. The scaling factors
534 represent the ratio of the estimated to true emissions. The ratio for the first guess is 0.5. The
535 actual value is 1.0. The pseudo-observations are produced by GC-Adjoint-HEMCO forward
536 simulation. The full modeled CO fields are used in OSSE-FullOBS as pseudo-CO observations.
537 The modeled CO fields are smoothed with MOPITT averaging kernels to produce MOPITT-
538 like pseudo-CO observations in OSSE-MOPITT.

539

540 **Table 4.** Regional anthropogenic CO emissions (with unit Tg/y) and annual scaling factors in
541 2015 in this work and Jiang et al. 2017.

542

543 **Fig. 1.** Framework to read the updated emission inventories in GC-Adjoint-HEMCO.

544

545 **Fig. 2.** Total combustion CO emissions in 2015 from (a) GC-v12; (b) GC-Adjoint-HEMCO;
546 (c) GC-Adjoint-STD. The unit is molec/cm²/s.

547

548 **Fig. 3.** Monthly variation in combustion CO emissions in 2015 from GC-v12, GC-Adjoint-
549 HEMCO and GC-Adjoint-STD.

550

551 **Fig. 4.** Averages of surface CO concentrations (unit ppbv) in 2015 from (a) GC-Adjoint-
552 HEMCO driven by MERRA-2, (b) GC-Adjoint-HEMCO driven by GEOS-FP and (c) their
553 difference; (d-f) same as panels a-c, but for CO columns (column-averaged dry-air mole
554 fractions, X_{co}).

555

556 **Fig. 5.** Averages of surface CO concentrations (unit ppbv) in 2015 from (a) GC-v12; (b) GC-
557 Adjoint-HEMCO; (c) GC-Adjoint-STD; (d-f) same as panels a-c, but for CO columns (column-
558 averaged dry-air mole fractions, X_{co}).

559

560 **Fig. 6.** Comparison of sensitivities of global CO concentrations to CO emission scaling factors
561 calculated using the adjoint method vs. the finite difference method. (a-c) the effects of
562 convection, PBL mixing and advection with 24-hour assimilation window; (d-f) the combined
563 effects (the advection process is turned off) with increased assimilation windows.

564

565 **Fig. 7.** (a) Annual scaling factors in OSSE-FullOBS. The scaling factors represent the ratio of
566 the estimated to true emissions. The ratio for the first guess is 0.5. The actual value is 1.0. (b-
567 c) the a priori and a posteriori biases calculated by (model-observation)/observation in OSSE-
568 Full. (d-f) same as panels a-c, but for OSSE-MOPITT.

569

570 **Fig. 8.** (a) Biases in monthly initial CO conditions in 2015 in the original GEOS-Chem
571 simulation. (b) same as panel a, but with optimized initial CO conditions provided by
572 suboptimal sequential Kalman filter. The biases are calculated by (model-MOPITT)/MOPITT.

573

574 **Fig. 9.** (a) A priori anthropogenic CO emissions in 2015 with unit molec/cm²/s; (b) Annual
575 scaling factors for CO emissions in 2015. The scaling factors represent the ratio of the estimated
576 to true emissions. (c-d) the a priori and a posteriori biases calculated by (model-
577 MOPITT)/MOPITT.

578

579 **References**

580 Barré, J., Edwards, D., Worden, H., Da Silva, A., and Lahoz, W.: On the feasibility of
581 monitoring carbon monoxide in the lower troposphere from a constellation of Northern
582 Hemisphere geostationary satellites. (Part 1), *Atmos Environ*, 113, 63-77,
583 10.1016/j.atmosenv.2015.04.069, 2015.

584 Dedoussi, I. C., Eastham, S. D., Monier, E., and Barrett, S. R. H.: Premature mortality related
585 to United States cross-state air pollution, *Nature*, 578, 261-265, 10.1038/s41586-020-1983-8,
586 2020.

587 Deeter, M. N., Edwards, D. P., Francis, G. L., Gille, J. C., Martínez-Alonso, S., Worden, H.
588 M., and Sweeney, C.: A climate-scale satellite record for carbon monoxide: the MOPITT
589 Version 7 product, *Atmos Meas Tech*, 10, 2533-2555, 10.5194/amt-10-2533-2017, 2017.

590 Fisher, J. A., Murray, L. T., Jones, D. B. A., and Deutscher, N. M.: Improved method for linear
591 carbon monoxide simulation and source attribution in atmospheric chemistry models
592 illustrated using GEOS-Chem v9, *Geosci Model Dev*, 10, 4129-4144, 10.5194/gmd-10-4129-
593 2017, 2017.

594 Guenther, A., Karl, T., Harley, P., Wiedinmyer, C., Palmer, P. I., and Geron, C.: Estimates of
595 global terrestrial isoprene emissions using MEGAN (Model of Emissions of Gases and
596 Aerosols from Nature), *Atmos Chem Phys*, 6, 3181-3210, 10.5194/acp-6-3181-2006, 2006.

597 Hammer, M. S., van Donkelaar, A., Li, C., Lyapustin, A., Sayer, A. M., Hsu, N. C., Levy, R.
598 C., Garay, M. J., Kalashnikova, O. V., Kahn, R. A., Brauer, M., Apte, J. S., Henze, D. K.,
599 Zhang, L., Zhang, Q., Ford, B., Pierce, J. R., and Martin, R. V.: Global Estimates and Long-
600 Term Trends of Fine Particulate Matter Concentrations (1998-2018), *Environ Sci Technol*,
601 54, 7879-7890, 10.1021/acs.est.0c01764, 2020.

602 Heald, C. L., Jacob, D. J., Jones, D. B. A., Palmer, P. I., Logan, J. A., Streets, D. G., Sachse,
603 G. W., Gille, J. C., Hoffman, R. N., and Nehr Korn, T.: Comparative inverse analysis of
604 satellite (MOPITT) and aircraft (TRACE-P) observations to estimate Asian sources of carbon
605 monoxide, *J Geophys Res-Atmos*, 109, D23306, 10.1029/2004jd005185, 2004.

606 Henze, D. K., Hakami, A., and Seinfeld, J. H.: Development of the adjoint of GEOS-Chem,
607 *Atmos Chem Phys*, 7, 2413-2433, 10.5194/acp-7-2413-2007, 2007.

608 Hoesly, R. M., Smith, S. J., Feng, L., Klimont, Z., Janssens-Maenhout, G., Pitkanen, T.,
609 Seibert, J. J., Vu, L., Andres, R. J., Bolt, R. M., Bond, T. C., Dawidowski, L., Kholod, N.,
610 Kurokawa, J.-i., Li, M., Liu, L., Lu, Z., Moura, M. C. P., O'Rourke, P. R., and Zhang, Q.:
611 Historical (1750–2014) anthropogenic emissions of reactive gases and aerosols from the
612 Community Emissions Data System (CEDS), *Geosci Model Dev*, 11, 369-408, 10.5194/gmd-
613 11-369-2018, 2018.

614 Jiang, Z., Jones, D. B. A., Worden, H. M., Deeter, M. N., Henze, D. K., Worden, J., Bowman,
615 K. W., Brenninkmeijer, C. A. M., and Schuck, T. J.: Impact of model errors in convective
616 transport on CO source estimates inferred from MOPITT CO retrievals, *J Geophys Res-
617 Atmos*, 118, 2073-2083, 10.1002/jgrd.50216, 2013.

618 Jiang, Z., Jones, D. B. A., Worden, J., Worden, H. M., Henze, D. K., and Wang, Y. X.: Regional
619 data assimilation of multi-spectral MOPITT observations of CO over North America, *Atmos
620 Chem Phys*, 15, 6801-6814, 10.5194/acp-15-6801-2015, 2015a.

621 Jiang, Z., Worden, J. R., Jones, D. B. A., Lin, J. T., Verstraeten, W. W., and Henze, D. K.:
622 Constraints on Asian ozone using Aura TES, OMI and Terra MOPITT, *Atmos Chem Phys*,
623 15, 99-112, 10.5194/acp-15-99-2015, 2015b.

624 Jiang, Z., Worden, J. R., Worden, H., Deeter, M., Jones, D. B. A., Arellano, A. F., and Henze,
625 D. K.: A 15-year record of CO emissions constrained by MOPITT CO observations, *Atmos
626 Chem Phys*, 17, 4565-4583, 10.5194/acp-17-4565-2017, 2017.

627 Jiang, Z., Zhu, R., Miyazaki, K., McDonald, B. C., Klimont, Z., Zheng, B., Boersma, K. F.,
628 Zhang, Q., Worden, H., Worden, J. R., Henze, D. K., Jones, D. B. A., Denier van der Gon,
629 H. A. C., and Eskes, H.: Decadal Variabilities in Tropospheric Nitrogen Oxides Over United
630 States, Europe, and China, *J Geophys Res-Atmos*, 127, e2021JD035872,
631 10.1029/2021jd035872, 2022.

632 Jones, D. B. A., Bowman, K. W., Palmer, P. I., Worden, J. R., Jacob, D. J., Hoffman, R. N.,
633 Bey, I., and Yantosca, R. M.: Potential of observations from the Tropospheric Emission
634 Spectrometer to constrain continental sources of carbon monoxide, *J Geophys Res-Atmos*,
635 108, 2003JD003702, 10.1029/2003jd003702, 2003.

636 Keller, C. A., Long, M. S., Yantosca, R. M., Da Silva, A. M., Pawson, S., and Jacob, D. J.:
637 HEMCO v1.0: a versatile, ESMF-compliant component for calculating emissions in
638 atmospheric models, *Geosci Model Dev*, 7, 1409-1417, 10.5194/gmd-7-1409-2014, 2014.

639 Kopacz, M., Jacob, D. J., Henze, D. K., Heald, C. L., Streets, D. G., and Zhang, Q.: Comparison
640 of adjoint and analytical Bayesian inversion methods for constraining Asian sources of carbon
641 monoxide using satellite (MOPITT) measurements of CO columns, *Journal of Geophysical
642 Research*, 114, D04305, 10.1029/2007jd009264, 2009.

643 Kuhns, H., Green, M., and Etyemezian, V.: Big Bend Regional Aerosol and Visibility
644 Observational (BRAVO) Study Emissions Inventory, Report prepared for BRAVO Steering
645 Committee, Desert Research Institute, Las Vegas, Nevada, 2003.

646 Li, K., Jacob, D. J., Liao, H., Shen, L., Zhang, Q., and Bates, K. H.: Anthropogenic drivers of
647 2013-2017 trends in summer surface ozone in China, *Proc Natl Acad Sci USA*, 116, 422-427,
648 10.1073/pnas.1812168116, 2019.

649 Li, M., Zhang, Q., Kurokawa, J.-i., Woo, J.-H., He, K., Lu, Z., Ohara, T., Song, Y., Streets, D.
650 G., Carmichael, G. R., Cheng, Y., Hong, C., Huo, H., Jiang, X., Kang, S., Liu, F., Su, H., and
651 Zheng, B.: MIX: a mosaic Asian anthropogenic emission inventory under the international
652 collaboration framework of the MICS-Asia and HTAP, *Atmos Chem Phys*, 17, 935-963,
653 10.5194/acp-17-935-2017, 2017.

654 Lin, H., Jacob, D. J., Lundgren, E. W., Sulprizio, M. P., Keller, C. A., Fritz, T. M., Eastham,
655 S. D., Emmons, L. K., Campbell, P. C., Baker, B., Saylor, R. D., and Montuoro, R.:
656 Harmonized Emissions Component (HEMCO) 3.0 as a versatile emissions component for
657 atmospheric models: application in the GEOS-Chem, NASA GEOS, WRF-GC, CESM2,
658 NOAA GEFS-Aerosol, and NOAA UFS models, *Geosci Model Dev*, 14, 5487-5506,
659 10.5194/gmd-14-5487-2021, 2021.

660 Qu, Z., Henze, D. K., Worden, H. M., Jiang, Z., Gaubert, B., Theys, N., and Wang, W.:
661 Sector - Based Top - Down Estimates of NO_x, SO₂, and CO Emissions in East Asia, *Geophys*
662 *Res Lett*, 49, e2021GL096009, 10.1029/2021gl096009, 2022.

663 Shu, L., Zhu, L., Bak, J., Zoogman, P., Han, H., Long, X., Bai, B., Liu, S., Wang, D., Sun, W.,
664 Pu, D., Chen, Y., Li, X., Sun, S., Li, J., Zuo, X., Yang, X., and Fu, T.-M.: Improved ozone
665 simulation in East Asia via assimilating observations from the first geostationary air-quality
666 monitoring satellite: Insights from an Observing System Simulation Experiment, *Atmos*
667 *Environ*, 274, 119003, 10.1016/j.atmosenv.2022.119003, 2022.

668 Tang, Z., Chen, J., and Jiang, Z.: Discrepancy in assimilated atmospheric CO over East Asia
669 in 2015–2020 by assimilating satellite and surface CO measurements, *Atmos Chem Phys*, 22,
670 7815-7826, 10.5194/acp-22-7815-2022, 2022.

671 Todling, R., and Cohn, S. E.: Suboptimal schemes for atmospheric data assimilation based on
672 the Kalman filter, *Monthly Weather Review*, 122, 10.1175/1520-
673 0493(1994)122<2530:SSFADA>2.0.CO;2, 1994.

674 van der Werf, G. R., Randerson, J. T., Giglio, L., Collatz, G. J., Mu, M., Kasibhatla, P. S.,
675 Morton, D. C., DeFries, R. S., Jin, Y., and van Leeuwen, T. T.: Global fire emissions and the
676 contribution of deforestation, savanna, forest, agricultural, and peat fires (1997–2009), *Atmos*
677 *Chem Phys*, 10, 11707-11735, 10.5194/acp-10-11707-2010, 2010.

678 Vestreng, V., and Klein, H.: Emission data reported to UNECE/EMEP. Quality assurance and
679 trend analysis and Presentation of WebDab, Norwegian Meteorological Institute, Oslo,
680 Norway, 2002.

681 Whaley, C. H., Strong, K., Jones, D. B. A., Walker, T. W., Jiang, Z., Henze, D. K., Cooke, M.
682 A., McLinden, C. A., Mittermeier, R. L., Pommier, M., and Fogal, P. F.: Toronto area ozone:
683 Long-term measurements and modeled sources of poor air quality events, *J Geophys Res-*
684 *Atmos*, 120, 11368-11390, 10.1002/2014JD022984, 2015.

685 Worden, H. M., Deeter, M. N., Edwards, D. P., Gille, J. C., Drummond, J. R., and Nédélec, P.:
686 Observations of near-surface carbon monoxide from space using MOPITT multispectral
687 retrievals, *Journal of Geophysical Research*, 115, D18314, 10.1029/2010jd014242, 2010.

688 Zhang, L., Chen, Y., Zhao, Y., Henze, D. K., Zhu, L., Song, Y., Paulot, F., Liu, X., Pan, Y.,
689 Lin, Y., and Huang, B.: Agricultural ammonia emissions in China: reconciling bottom-up and
690 top-down estimates, *Atmos Chem Phys*, 18, 339-355, 10.5194/acp-18-339-2018, 2018.

691 Zhang, Q., Streets, D. G., Carmichael, G. R., He, K. B., Huo, H., Kannari, A., Klimont, Z.,
692 Park, I. S., Reddy, S., Fu, J. S., Chen, D., Duan, L., Lei, Y., Wang, L. T., and Yao, Z. L.:
693 Asian emissions in 2006 for the NASA INTEX-B mission, *Atmos Chem Phys*, 9, 5131-5153,
694 10.5194/acp-9-5131-2009, 2009.

695 Zhao, H., Geng, G., Zhang, Q., Davis, S. J., Li, X., Liu, Y., Peng, L., Li, M., Zheng, B., Huo,
696 H., Zhang, L., Henze, D. K., Mi, Z., Liu, Z., Guan, D., and He, K.: Inequality of household
697 consumption and air pollution-related deaths in China, *Nat Commun*, 10, 4337,
698 10.1038/s41467-019-12254-x, 2019.

699 Zhu, C., Byrd, R. H., Lu, P., and Nocedal, J.: Algorithm 778: L-BFGS-B: Fortran Subroutines
700 for Large-Scale Bound Constrained Optimization, *ACM Transactions on Mathematical*
701 *Software*, 23, 550-560, 10.1145/279232.279236, 1997.

702

Inventories	GC-v12	GC-Adjoint- HEMCO	Inventories	GC-Adjoint- STD
CEDS	613.57	613.85	GEIA	445.88
MIX	321.18	321.71	INTEX-B	353.03
NEI2011	35.83	37.70	NEI2008	52.87
DICE_AF + AF_EDGAR43	83.42	83.02	\	\
APEI	6.10	6.17	CAC	10.20
GFED4	437.13	435.89	GFED3	382.04

Table 1. CO emissions for each inventory in 2015 with unit Tg/y.

Version Region	Combustion Emission (Tg/y)			PCO_NMVOC (kg/s)			PCO_CH4 (kg/s)		
	GC-v12	GC- Adjoint- HEMCO	GC- Adjoint- STD	GC-v12	GC- Adjoint- HEMCO	GC- Adjoint- STD	GC-v12	GC- Adjoint- HEMCO	GC- Adjoint- STD
Asia	320.66	320.38	331.65	15.49	15.52	22.37	14.21	14.40	10.67
North America	73.96	66.93	60.65	7.05	6.83	14.75	7.45	7.66	5.23
Africa	199.51	193.29	179.22	34.57	33.92	52.38	19.57	19.85	16.18
South America	79.04	78.91	75.82	44.15	42.55	74.64	17.14	17.42	14.08
Europe	31.58	30.96	48.48	4.20	4.14	10.17	7.13	7.41	4.58
Australia	12.24	11.99	22.87	21.23	20.68	48.89	13.88	14.62	10.67
Version Region	CO_OH (kg/s)			CO (surface ppbv)			CO (column xco)		
	GC-v12	GC- Adjoint- HEMCO	GC- Adjoint- STD	GC-v12	GC- Adjoint- HEMCO	GC- Adjoint- STD	GC-v12	GC- Adjoint- HEMCO	GC- Adjoint- STD
Asia	52.26	51.34	40.87	179.56	184.29	187.90	90.23	88.16	89.58
North America	23.02	22.57	16.20	120.38	113.49	108.27	79.16	76.27	71.35
Africa	63.78	61.84	51.03	133.56	127.38	141.97	84.26	81.52	86.36
South America	49.06	48.85	41.25	107.98	106.16	132.24	72.93	70.67	78.75
Europe	20.65	20.92	14.27	112.88	111.33	120.09	74.83	72.34	70.45
Australia	31.42	31.98	25.27	67.45	65.00	84.80	56.35	54.02	61.15

Table 2. Regional combustion CO emissions, VOC-generated CO (PCO_NMVOC), CH₄-generated CO (PCO_CH₄), CO sinks (CO_OH, calculated as CO_OH = KRATE×CO×OH), and simulated surface and column CO concentrations in 2015. The region definitions are shown in Fig. 2A.

	Scaling Factors OSSE-FullOBS	Scaling Factors OSSE-MOPITT
Asia	1.00	1.04
North America	0.97	0.88
Africa	0.97	1.01
South America	1.00	1.02
Europe	0.98	0.84
Australia	0.94	0.81

Table 3. Annual scaling factors of anthropogenic CO emissions in OSSEs. The scaling factors represent the ratio of the estimated to true emissions. The ratio for the first guess is 0.5. The actual value is 1.0. The pseudo-observations are produced by GC-Adjoint-HEMCO forward simulation. The full modeled CO fields are used in OSSE-FullOBS as pseudo-CO observations. The modeled CO fields are smoothed with MOPITT averaging kernels to produce MOPITT-like pseudo-CO observations in OSSE-MOPITT.

		Asia	North America	Africa	South America	Europe	Australia
This work	A priori CO emissions	243.53	34.42	23.24	30.39	25.94	2.02
	A posteriori CO emissions	283.20	50.47	35.34	42.92	41.62	2.79
	Scaling Factors	1.16	1.47	1.52	1.41	1.60	1.38
Jiang et al. 2017	A priori CO emissions	270.50	43.70	29.39	17.47	44.45	0.83
	A posteriori CO emissions	205.40	47.06	35.04	16.67	53.58	0.82
	Scaling Factors	0.76	1.08	1.19	0.95	1.21	0.99

Table 4. Regional anthropogenic CO emissions (with unit Tg/y) and annual scaling factors in 2015 in this work and Jiang et al. 2017.

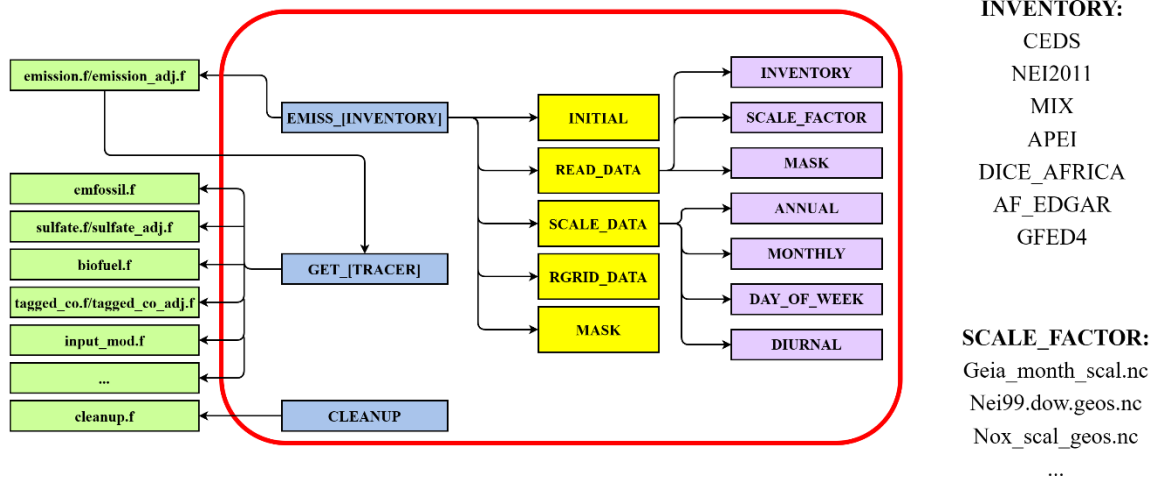


Fig. 1. Framework to read the updated emission inventories in GC-Adjoint-HEMCO.

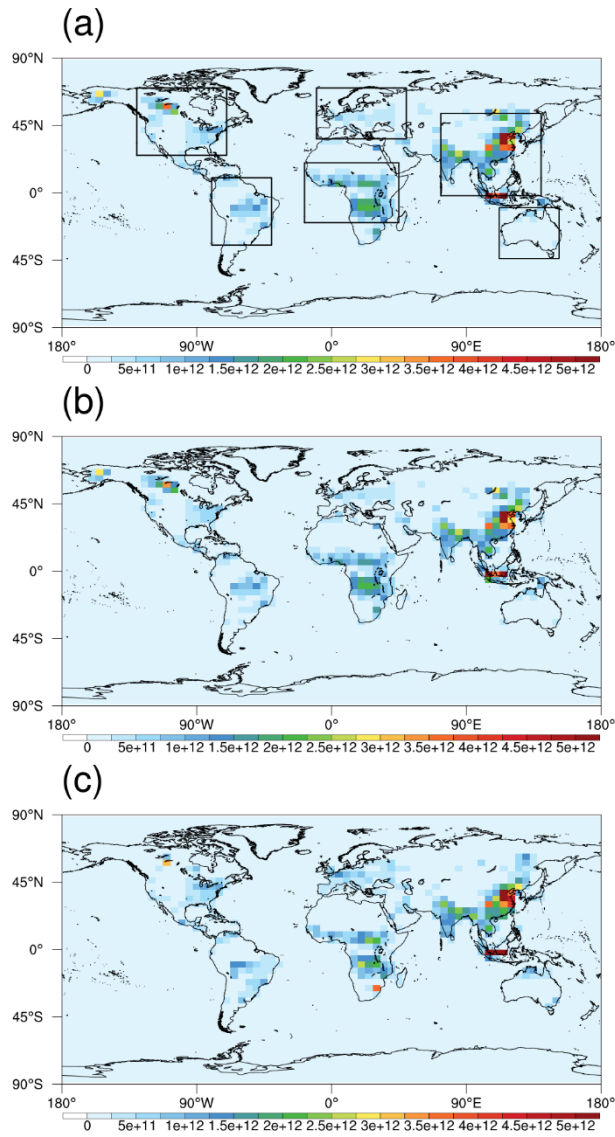


Fig. 2. Total combustion CO emissions in 2015 from (a) GC-v12; (b) GC-Adjoint-HEMCO; (c) GC-Adjoint-STD. The unit is $\text{molec}/\text{cm}^2/\text{s}$.

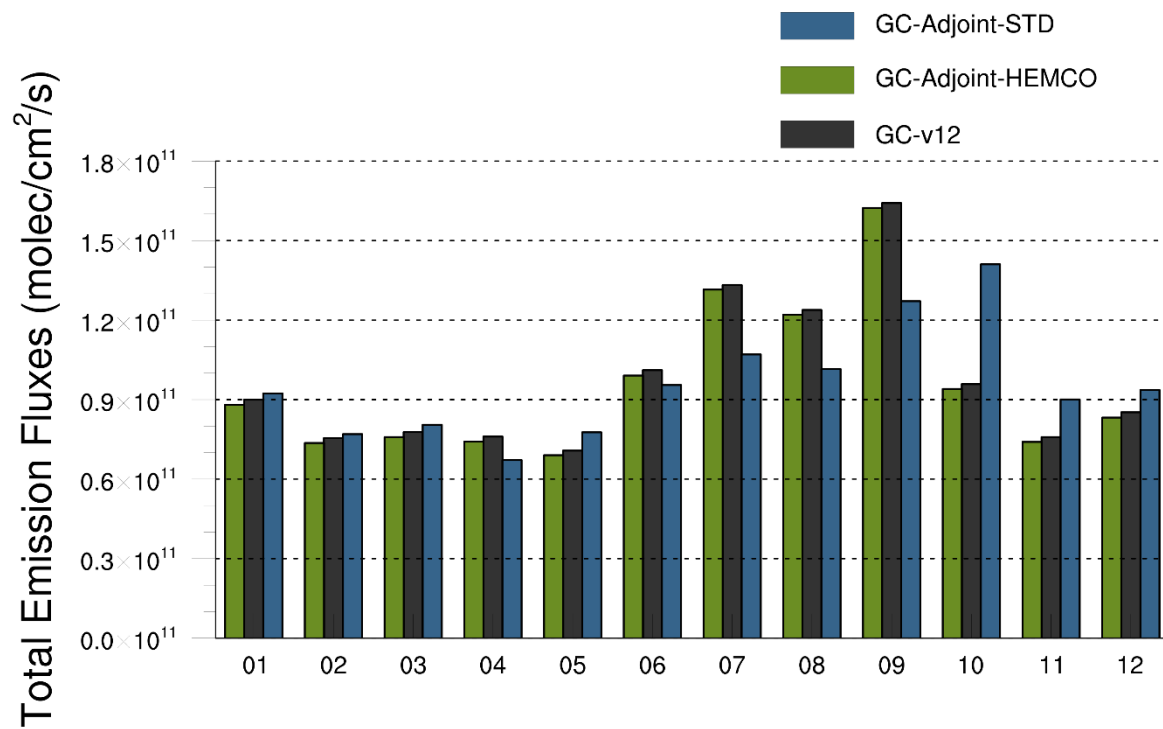


Fig. 3. Monthly variation in combustion CO emissions in 2015 from GC-v12, GC-Adjoint-HEMCO and GC-Adjoint-STD.

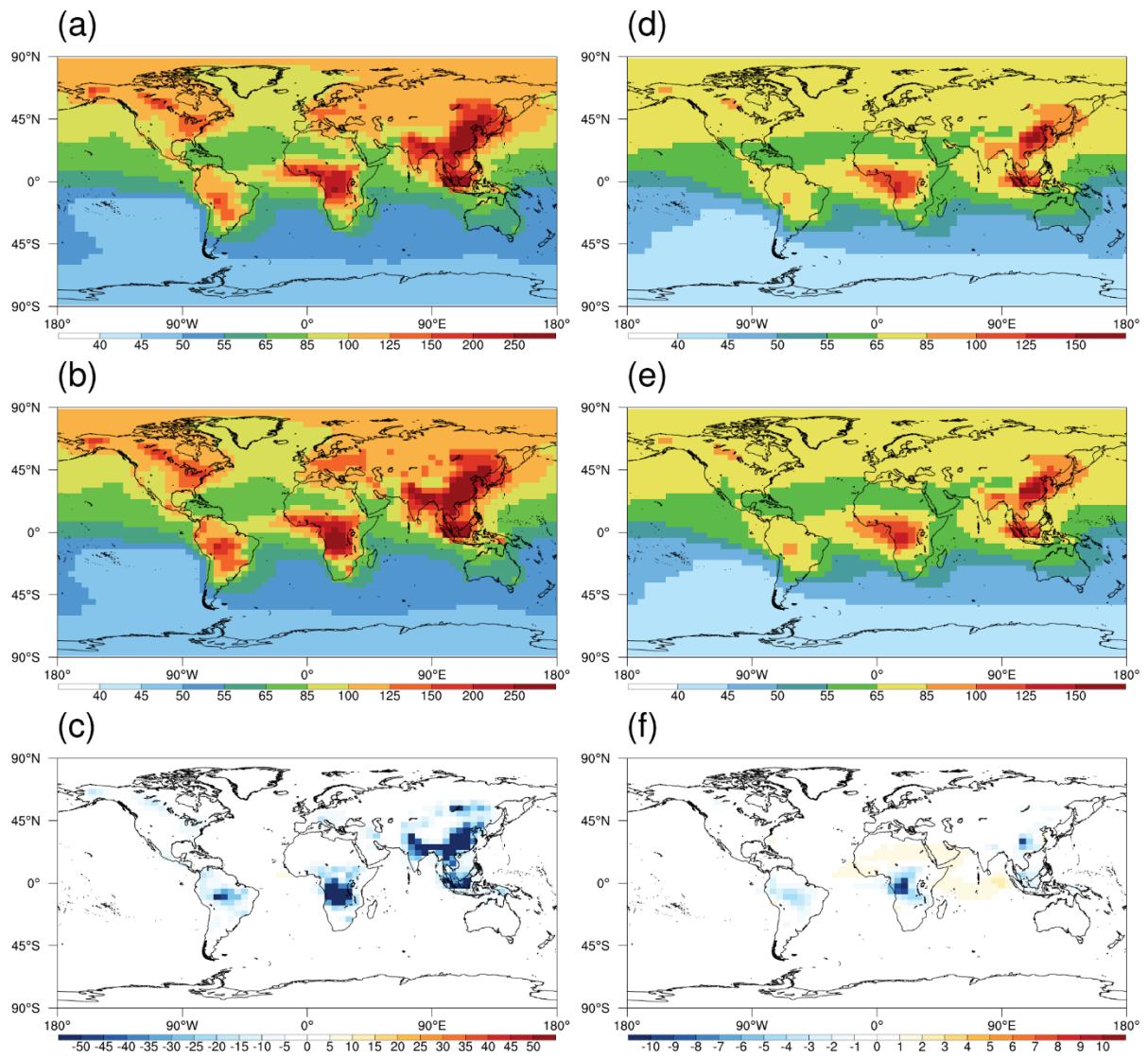


Fig. 4. Averages of surface CO concentrations (unit ppbv) in 2015 from (a) GC-Adjoint-HEMCO driven by MERRA-2, (b) GC-Adjoint-HEMCO driven by GEOS-FP and (c) their difference; (d-f) same as panels a-c, but for CO columns (column-averaged dry-air mole fractions, X_{CO}).

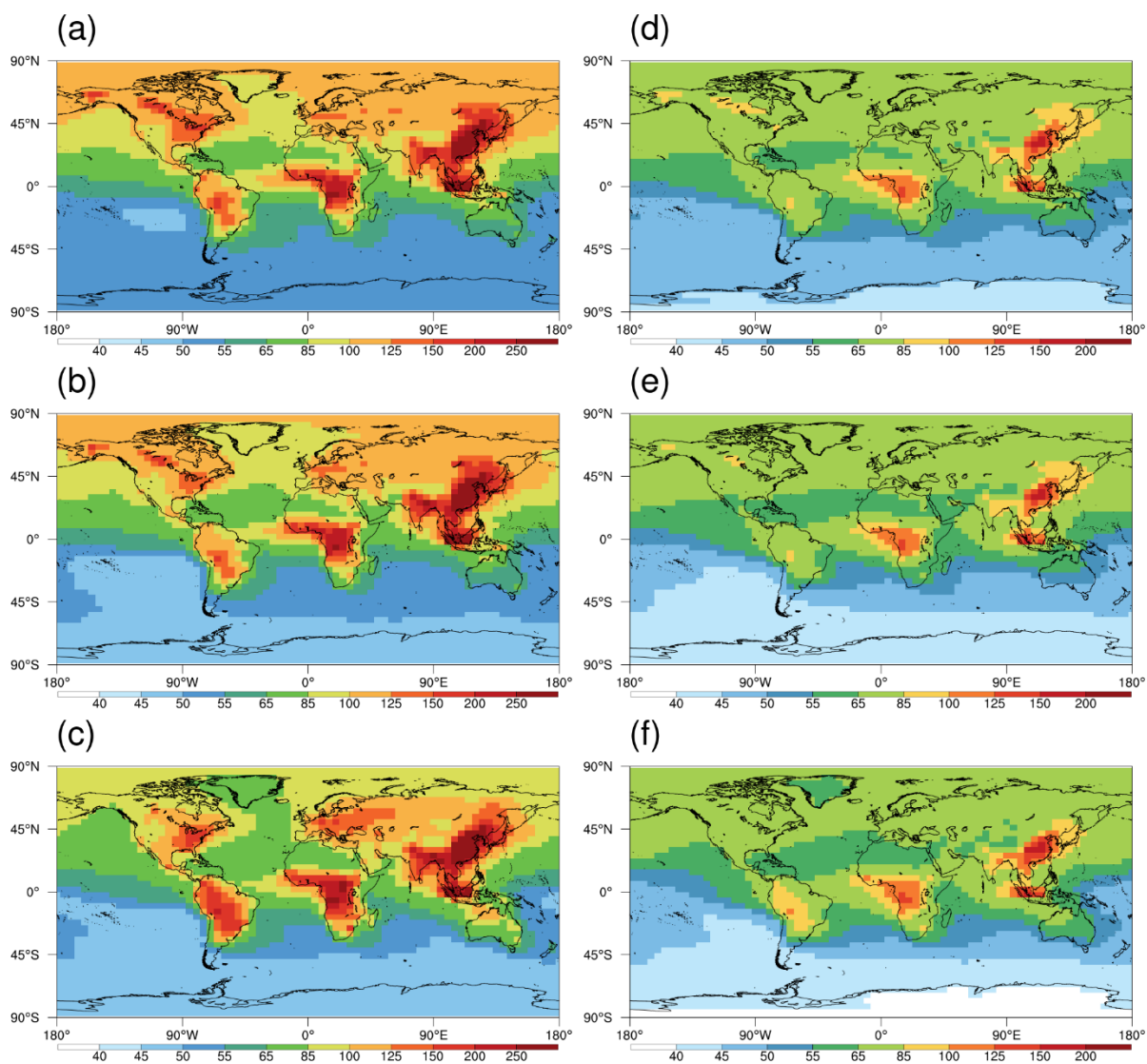


Fig. 5. Averages of surface CO concentrations (unit ppbv) in 2015 from (a) GC-v12; (b) GC-Adjoint-HEMCO; (c) GC-Adjoint-STD; (d-f) same as panels a-c, but for CO columns (column-averaged dry-air mole fractions, X_{co}).

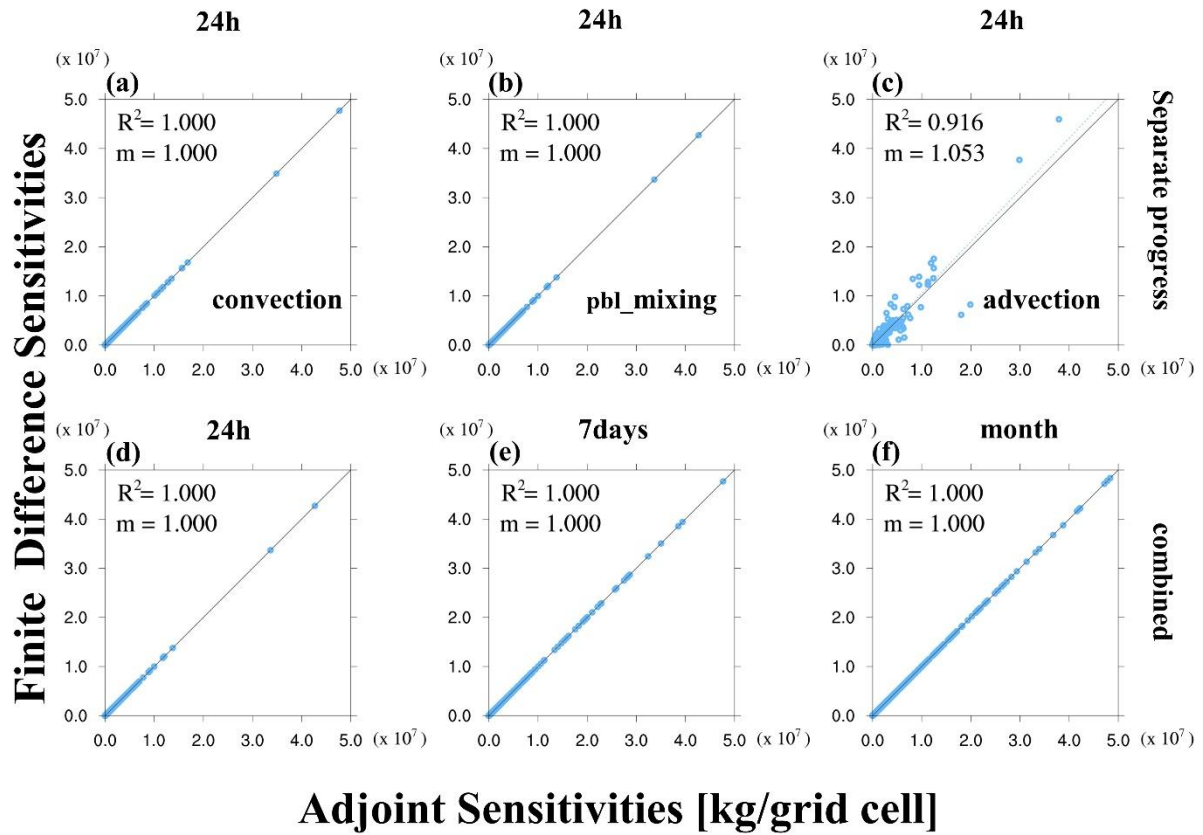


Fig. 6. Comparison of sensitivities of global CO concentrations to CO emission scaling factors calculated using the adjoint method vs. the finite difference method. (a-c) the effects of convection, PBL mixing and advection with 24-hour assimilation window; (d-f) the combined effects (the advection process is turned off) with increased assimilation windows.

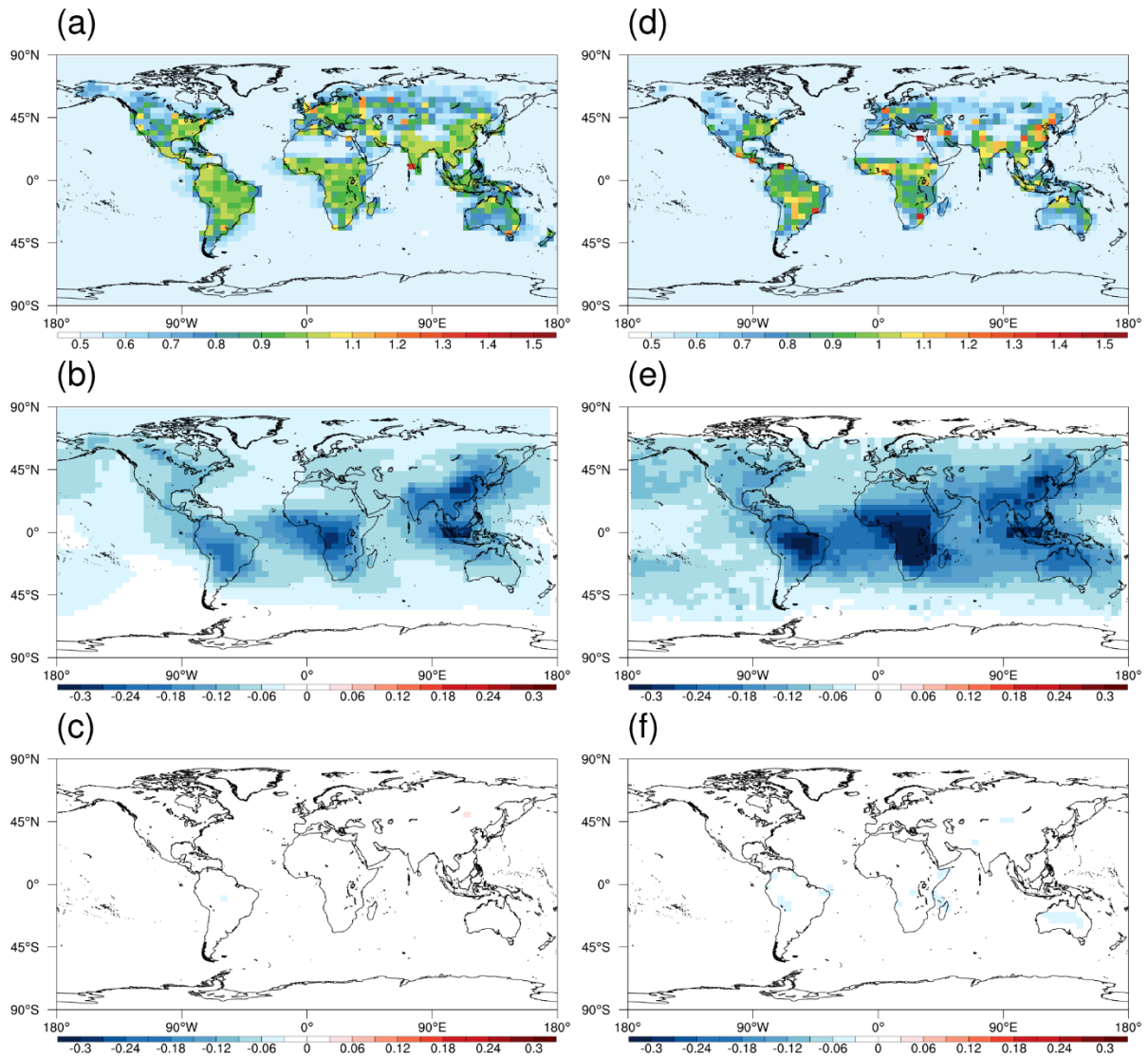


Fig. 7. (a) Annual scaling factors in OSSE-FullOBS. The scaling factors represent the ratio of the estimated to true emissions. The ratio for the first guess is 0.5. The actual value is 1.0. (b-c) the a priori and a posteriori biases calculated by (model-observation)/observation in OSSE-Full. (d-f) same as panels a-c, but for OSSE-MOPITT.

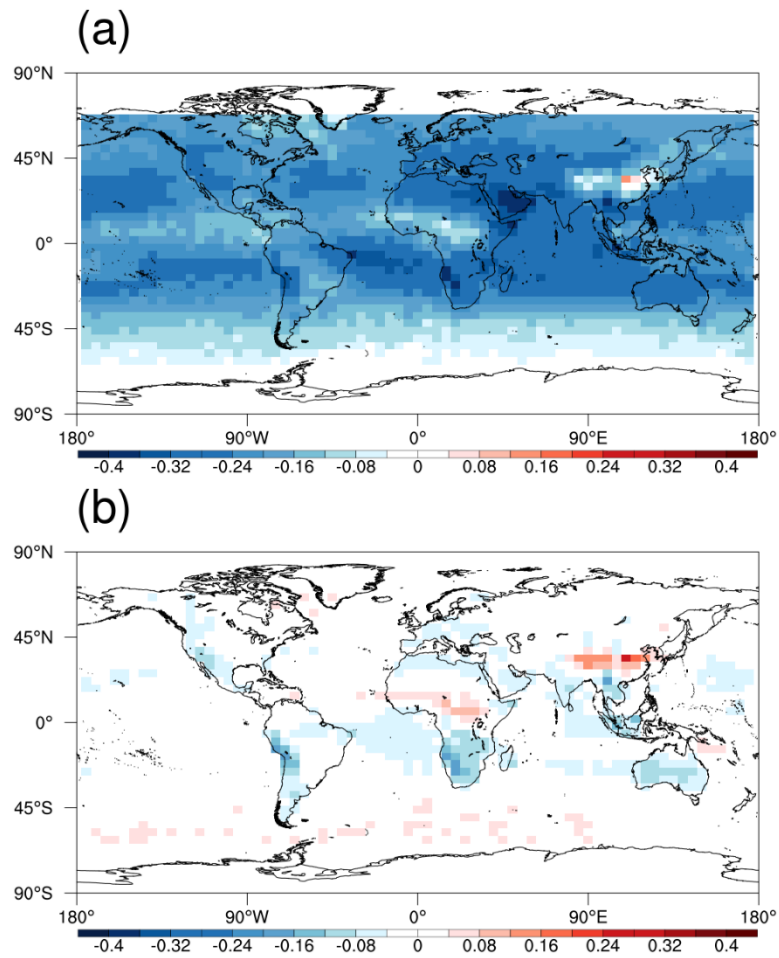


Fig. 8. (a) Biases in monthly initial CO conditions in 2015 in the original GEOS-Chem simulation. (b) same as panel a, but with optimized initial CO conditions provided by suboptimal sequential Kalman filter. The biases are calculated by $(\text{model-MOPITT})/\text{MOPITT}$.

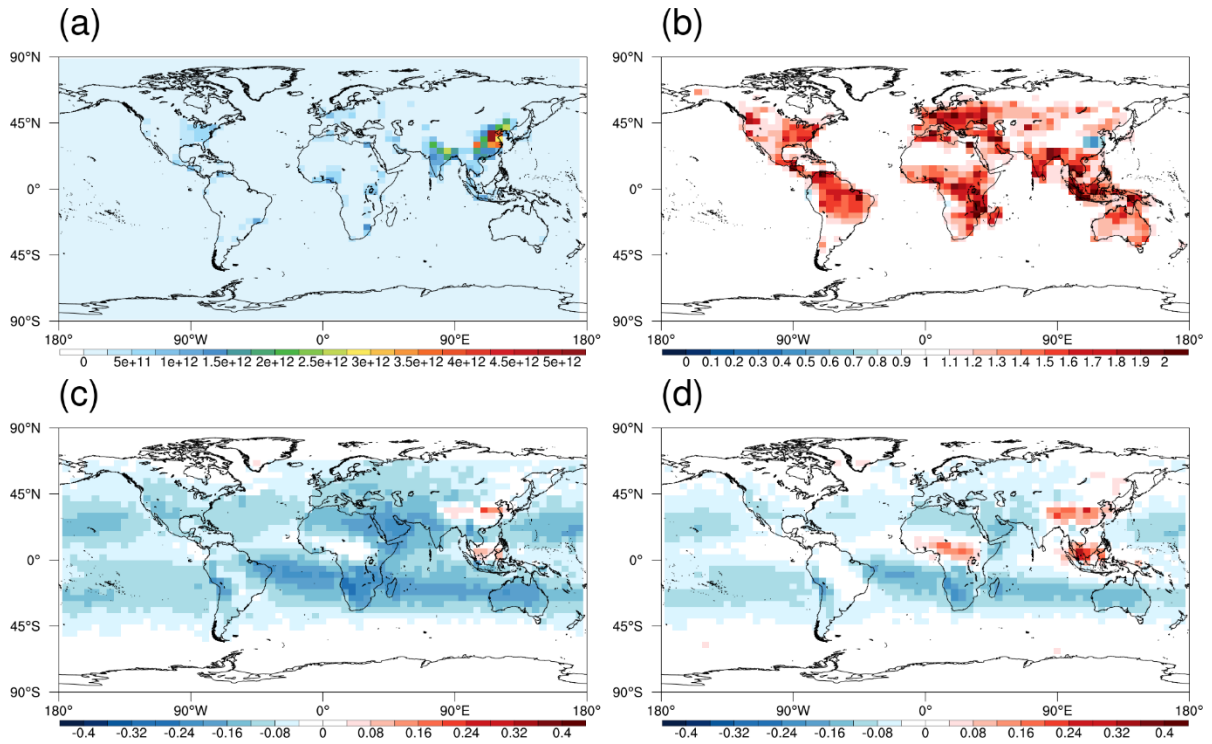


Fig. 9. (a) A priori anthropogenic CO emissions in 2015 with unit molec/cm²/s; (b) Annual scaling factors for CO emissions in 2015. The scaling factors represent the ratio of the estimated to true emissions. (c-d) the a priori and a posteriori biases calculated by (model-MOPITT)/MOPITT.